

Density dependence of the symmetry energy and the nuclear equation of state: A Dynamical and Statistical model perspective

D.V. Shetty, S.J. Yennello, and G.A. Souliotis
Cyclotron Institute, Texas A&M University, College Station, TX 77843, USA
 (Dated: October 25, 2018)

The density dependence of the symmetry energy in the equation of state of isospin asymmetric nuclear matter is of significant importance for studying the structure of systems as diverse as the neutron-rich nuclei and the neutron stars. A number of reactions using the dynamical and the statistical models of multifragmentation, and the experimental isoscaling observable, is studied to extract information on the density dependence of the symmetry energy. It is observed that the dynamical and the statistical model calculations give consistent results assuming the sequential decay effect in dynamical model to be small. A comparison with several other independent studies is also made to obtain important constraint on the form of the density dependence of the symmetry energy. The comparison rules out an extremely “stiff” and “soft” form of the density dependence of the symmetry energy with important implications for astrophysical and nuclear physics studies.

PACS numbers: 21.30.Fe, 25.70.-z, 25.70.Lm, 25.70.Mn, 25.70.Pq

I. INTRODUCTION

The fundamental goal of nuclear physics is to understand the basic building blocks of nature - neutrons and protons - and the nature of interaction that binds them together into nuclear matter. Studying the nature of matter and the strength of nuclear interaction is key to understanding some of the fundamental problems such as, How are elements formed? How do stars explode into supernova? What kind of matter exists inside a neutron star? How are neutrons compressed inside a neutron star to density trillions of times greater than on earth? What determines the density-pressure relation, the so-called equation of state?

The key ingredient for constructing the nuclear equation of state is the basic nucleon-nucleon interaction. Until now our understanding of the nucleon-nucleon interaction has come from studying nuclear matter that is symmetric in isospin (neutron-to-proton ratio, $N/Z \approx 1$) and matter found near normal nuclear density ($\rho_0 \approx 0.16 \text{ fm}^{-3}$). It is not known how far this understanding remains valid as one goes away from the normal nuclear density and symmetric nuclear matter. Various interactions used in “ab initio” microscopic calculations predict different forms of the nuclear equation of state above and below the normal nuclear matter density, and away from the symmetric nuclear matter [1, 2, 3, 4, 5, 6]. As a result, the symmetry energy, which is the difference in energy between the pure neutron matter and the symmetric nuclear matter, shows very different behavior above and below normal nuclear density [6] (see Fig. 1).

In general, two different forms of the density dependence of the symmetry energy have been predicted. One, where the symmetry energy increases monotonically with increasing density (“stiff” dependence) and the other, where the symmetry energy increases initially up to normal nuclear density and then decreases at higher densities (“soft” dependence). Constraining the form of the density dependence of the symmetry energy is important not

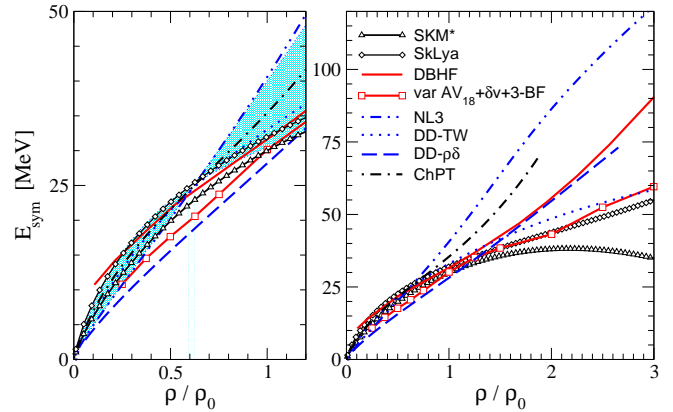


FIG. 1: (Color online) Symmetry energy as a function of density predicted by microscopic “ab initio” calculations. The left panel shows the low-density region, while the right panel displays the high-density range. The figure is taken from Ref. [6].

only for a better understanding of the nucleon-nucleon interaction, and hence its extrapolation to the structure of neutron-rich nuclei [7, 8, 9, 10], but also for determining the structure of compact stellar objects such as neutron stars [11, 12, 13, 14, 15, 16, 17]. For example, a “stiff” form of the density dependence of the symmetry energy is predicted to lead to a large neutron skin thickness compared to a “soft” dependence [8, 10, 18, 19, 20]. Similarly, a “stiff” dependence of the symmetry energy can result in rapid cooling of a neutron star, and a larger neutron star radius, compared to a “soft” density dependence of the symmetry energy [20, 21, 22]. The nuclear Equation Of State (EOS) is therefore a fundamental entity that determines the properties of systems as diverse as atomic nuclei and neutron stars, and the knowledge of which is of significant importance [16, 17, 23].

Experimentally, the best possible means of studying the nuclear equation of state at sub-normal nuclear den-

sity is through intermediate-energy heavy-ion reactions [26, 27]. In this kind of reaction, an excited nucleus (the composite of the projectile and the target nucleus) expands to a sub-nuclear density and disintegrates into various light and heavy fragments in a process called multifragmentation. By studying the isotopic yield distribution of these fragments one can extract important information about the symmetry energy and its density dependence. Current studies on the nuclear equation of state are limited to beams consisting of stable nuclei. It is hoped that in the future radioactive beam facilities such as, FAIR (GSI) [24], SPIRAL2 (GANIL) and FRIB (USA) [25] will provide tremendous opportunities for exploring the nuclear EOS in regions never before studied (*i.e.*, extreme isospin and away from normal nuclear density).

In this work, we have made an attempt to study the density dependence of the symmetry energy using two different theoretical approaches for studying multifragmentation, namely the dynamical and the statistical model approaches of multifragmentation. In section II, the isoscaling technique used to study the density dependence of the symmetry energy, and their different interpretations in terms of statistical and dynamical approach, are presented. In section III and IV, a brief description of the experiment and the experimental results are presented. The dynamical and the statistical approaches used to interpret the experimental results are presented in section V. A comparison between the two approaches with other independent studies is presented in section VI. Finally, a discussion and summary, and conclusions are presented in section VII and VIII, respectively.

II. SYMMETRY ENERGY AND THE ISOTOPIC YIELD DISTRIBUTION

It has been shown from experimental measurements that the ratio of the fragment yields, $R_{21}(N, Z)$, taken from two different multifragmentation reactions, 1 and 2, obeys an exponential dependence on the neutron number (N) and the proton number (Z) of the fragments; an observation known as isoscaling [28, 29, 30]. The dependence is characterized by the relation,

$$R_{21}(N, Z) = Y_2(N, Z)/Y_1(N, Z) = C e^{(\alpha N + \beta Z)} \quad (1)$$

Where, Y_2 and Y_1 are the fragment yields from the neutron-rich and the neutron-deficient systems, respectively. C is an overall normalization factor, and α and β are the parameters characterizing the isoscaling behavior. Isoscaling is also theoretically predicted by the dynamical [31, 32, 33, 34, 35] and statistical [36, 37, 38, 39] models of multifragmentation. In these models, the difference in the chemical potential of systems with different neutron-to-proton ration (N/Z) is directly related to the isoscaling parameter α . The isoscaling parameter α , is

related to the symmetry energy C_{sym} , through the relation,

$$\alpha = \frac{4C_{sym}}{T} \left(\frac{Z_1^2}{A_1^2} - \frac{Z_2^2}{A_2^2} \right) \quad (2)$$

where, Z_1 , A_1 and Z_2 , A_2 are the charge and the mass numbers from the two systems and T is the temperature. This relation provides a simple and straight-forward connection between the symmetry energy and the fragment isotopic yield distribution.

It must be mentioned that although the above equation derived from the statistical and the dynamical models of multifragmentation appears similar in form, the physical meaning of the terms involved in this equation differ for each model.

1) In statistical models, the Z/A in Eq. (2) corresponds to the charge-to-mass ratio of the initial equilibrated fragmenting system. Whereas, in dynamical models, it corresponds to the charge-to-mass ratio of the liquid phase at a certain time (≈ 300 fm/c) during the dynamical evolution of the colliding systems.

2) The interpretation of the symmetry energy C_{sym} , in dynamical and statistical models also differs significantly. The dynamical models relate the symmetry energy in the above equation to that of the fragmenting source. The statistical models, on the other hand, relate C_{sym} to that of the fragments formed at freeze-out.

These conceptual differences between the statistical and the dynamical models are due to the radically different approaches taken in the interpretation of the multifragmentation process. The different interpretation has also lead to conflicting results from the use of Eq. 2, due to the different sequential decay effects predicted for the primary fragments by each model.

The isoscaling parameter α , in Eq. 2 corresponds to the hot primary fragments which undergo sequential decay into cold secondary fragments. These secondary fragments are the ones that are eventually detected in experiments. The experimentally determined isoscaling parameter must therefore be corrected for the sequential decay effect before comparing it to the theoretical models. It has been observed that while statistical model calculations show no significant change in the isoscaling parameter after sequential decay [40], dynamical models give contrasting results; with some showing no significant changes [41], while others showing a change of as much as 50% [42].

In this work, we adopt both theoretical approaches with their respective interpretations to study the density dependence of the symmetry energy. In particular, we use the Antisymmetrized Molecular Dynamics (AMD) model [31, 43] and the Statistical Multifragmentation Model (SMM) [36] for this study. A comparison between the two can provide useful insight into the physical meaning of the above equation in the two models.

III. EXPERIMENT

A. Experimental Setup

The experiments were carried out at the Cyclotron Institute of Texas A&M University (TAMU) using the K500 Superconducting Cyclotron and the National Superconducting Cyclotron Laboratory (NSCL) at Michigan State University (MSU). Targets of ^{58}Fe (2.3 mg/cm²) and ^{58}Ni (1.75 mg/cm²) were bombarded with beams of ^{40}Ar and ^{40}Ca at 33 and 45 MeV/nucleon for the TAMU measurements [44], and targets of ^{58}Fe (~ 5 mg/cm²) and ^{58}Ni (~ 5 mg/cm²) were bombarded with beams of ^{40}Ar and ^{40}Ca at 25 and 53 MeV/nucleon for the NSCL measurements [45]. The various combinations of target and projectile nuclei allowed for a range of N/Z (neutron-to-proton ratio) (1.04 – 1.23) of the system to be studied, while keeping the total mass constant ($A = 98$). In a separate experiment at TAMU, beams of ^{58}Ni and ^{58}Fe at 30, 40, and 47 MeV/nucleon were also bombarded on self-supporting ^{58}Ni and ^{58}Fe targets.

The beams in the TAMU measurements were fully stripped by allowing them to pass through a thin aluminum foil before being hit at the center of the target inside the TAMU 4π neutron ball [46]. Light charged particles ($Z \leq 2$) and intermediate mass fragments ($Z > 2$) were detected using six discrete telescopes placed inside the scattering chamber of the neutron ball at angles of 10°, 44°, 72°, 100°, 128° and 148°. Each telescope consisted of a gas ionization chamber (IC) followed by a pair of silicon detectors (Si-Si) and a CsI scintillator detector, providing three distinct detector pairs (IC-Si, Si-Si, and Si-CsI) for fragment identification. The ionization chamber was of axial field design and was operated with CF₄ gas at a pressure of 50 Torr. The gaseous medium was 6 cm thick with a typical threshold of ~ 0.5 MeV/nucleon for intermediate mass fragments. The silicon detectors had an active area of 5 cm \times 5 cm and were each subdivided into four quadrants. The first and second silicon detectors in the stack were 0.14 mm and 1 mm thick, respectively. The dynamical energy range of the silicon pair was $\sim 16 - 50$ MeV for ^4He and $\sim 90 - 270$ MeV for ^{12}C . The CsI scintillator crystals that followed the silicon detector pair were 2.54 cm in thickness and were read out by photodiodes. Good elemental (Z) identification was achieved for fragments that punched through the IC detector and stopped in the first silicon detector. Fragments measured in the Si-Si detector pair also had good isotopic separation. Fragments that stopped in CsI detectors showed isotopic resolution up to $Z = 7$. The trigger for the data acquisition was generated by requiring a valid hit in one of the silicon detectors.

The calibration of the IC-Si detectors were carried out using the standard alpha sources and by operating the IC at various gas pressures. The Si-Si detectors were calibrated by measuring the energy deposited by the alpha particles in the thin silicon and the punch-through energies of different isotopes in the thick silicon. The Si-CsI

detectors were calibrated by selecting points along the different light charged isotopes and determining the energy deposited in the CsI crystal from the energy loss in the calibrated Si detector.

The setup for the NSCL experiment consisted of 13 silicon detector telescopes placed inside the MSU 4π Array. Four of which were placed at 14°, each of which consisted of a 100 μm thick and a 1 mm thick silicon surface-barrier detector followed by a 20 cm thick plastic scintillator. Five telescopes were placed at 40°, in front of the most forward detectors in the main ball of the 4π Array. They each consisted of a 100 μm surface-barrier detector followed by a 5 mm lithium drifted silicon detector. More details can be found in Ref. [45]. Good isotopic resolution was obtained as in TAMU measurements.

B. Event Characterization

The event characterization of the NSCL data was accomplished by detection of nearly all the coincident charged particles by the MSU 4π Array. Data were acquired using two different triggers; the bulk of which was obtained with the requirement of a valid event in one of the silicon telescopes. Additional data were taken with a minimum bias 4π Array trigger for normalization of the event characterization. The impact parameter of the event was determined by the mid-rapidity charge detected in the 4π Array as discussed in Ref. [47]. The effectiveness of the centrality cuts was tested by comparing the multiplicity of events from a minimum bias trigger with the multiplicity distribution when a valid fragment was detected at 40° [48]. The minimum bias trigger had a peak multiplicity of charged particles of one, whereas with the requirement of a fragment at 40°, the peak of the multiplicity distribution increased to five.

The event characterization for the TAMU data was accomplished by using the 4π neutron ball that surrounded the detector assembly. The neutron ball consisted of eleven scintillator tanks segmented in its median plane and surrounding the vacuum chamber. The upper and the lower tank were 1.5 m diameter hemispheres. Nine wedge-shaped detectors were sandwiched between the hemispheres. All the wedges subtended 40° in the horizontal plane. The neutron ball was filled with a pseudocumene-based liquid scintillator mixed with 0.3 % (b.w.) of Gd salt (Gd 2-ethyl hexanoate). Scintillations from thermal neutrons captured by Gd were detected by twenty 5-inch phototubes : five in each hemisphere, one on each of the identical 40° wedges and two on the forward edges. The efficiency with which the neutrons could be detected is about 83%, as measured with a ^{252}Cf source.

The detected neutrons were used to differentiate between the central and peripheral collisions. To understand the effectiveness of neutron multiplicity as a centrality trigger, simulations were carried out us-

ing a hybrid BUU-GEMINI calculations at various impact parameters for the $^{40}\text{Ca} + ^{58}\text{Fe}$ reaction at 33 MeV/nucleon. The simulated neutron multiplicity distribution was compared with the experimentally measured distribution. The multiplicity of neutron for the impact parameter $b = 0$ collisions was found to be higher than the $b = 5$ collision. By gating on the 10% highest neutron multiplicity events, one could clearly discriminate against the peripheral events.

To determine the contributions from noncentral impact parameter collisions, neutrons emitted in coincidence with fragments at 44° and 152° were calculated at $b = 0$ fm and $b = 5$ fm. The number of events were adjusted for geometrical cross sectional differences. A ratio was made between the number of events with a neutron multiplicity of at least six, calculated at $b = 0$ fm, and the number of events with the same neutron multiplicity at $b = 5$ fm. The ratios were observed to be 19.0 and 11.1 at 44° and 1.3 and 2.2 at 152° for 33 and 45 MeV/nucleon respectively. At intermediate angles, high neutron multiplicities were observed to be outside the region in which $b = 5$ fm contributes significantly. At backward angles the collisions at $b = 5$ fm made a larger contribution to the neutron multiplicity.

In addition to the neutron multiplicity distribution, the charge distribution of the fragments was also used to investigate the contributions from central and mid-impact parameter collisions. The $b = 5$ collisions produced essentially no fragments with charge greater than three in the 44° telescope.

In an earlier work [44], some analysis of the fragment kinetic energy and charge distributions were presented. It was shown that at a laboratory angle of 44° the kinetic energy and the charge distributions are well reproduced by the statistical model calculation. Using a moving source analysis of the fragment energy spectra, it was also shown that the fragments emitted at backward angles originate from a target-like source, while those emitted at 44° originate primarily from a composite source. In this work, we will concentrate exclusively on data from the laboratory angle of 44° , which corresponds to the center of mass angle $\approx 90^\circ$, to study the symmetry energy and the isoscaling properties of the fragments produced. The choice of this angle enables one to select events which are predominantly central and undergo bulk multifragmentation. The contributions to the intermediate mass fragments from the projectile-like and target-like sources can therefore be assumed to be minimal.

IV. EXPERIMENTAL RESULTS

A. Fragment isotopic yield distribution

The experimentally measured relative isotopic yield distributions for the Lithium (left) and Carbon (right) elements, in $^{58}\text{Ni} + ^{58}\text{Ni}$ (star symbols), $^{58}\text{Ni} + ^{58}\text{Fe}$ (square symbols), $^{58}\text{Fe} + ^{58}\text{Ni}$ (circle symbols) and $^{58}\text{Fe} + ^{58}\text{Fe}$ (triangle symbols) reactions, are shown in Fig. 2 for beam energies of 30, 40 and 47 MeV/nucleon. Similarly, the isotopic yield distributions for Lithium (left), Beryllium (center) and Carbon (right) elements, in $^{40}\text{Ca} + ^{58}\text{Ni}$ (star symbols), $^{40}\text{Ar} + ^{58}\text{Ni}$ (circle symbols) and $^{40}\text{Ar} + ^{58}\text{Fe}$ (square symbols) reactions, are shown in figure 3 for beam energies of 25, 33 and 45 MeV/nucleon. The isotope distribution for each element in Fig. 3 shows higher fragment yield for the neutron rich isotopes in $^{40}\text{Ar} + ^{58}\text{Fe}$ reaction (squares), which has the largest neutron-to-proton ratio (N/Z), in comparison to the $^{40}\text{Ca} + ^{58}\text{Ni}$ reaction (stars), which has the smallest neutron-to-proton ratio. The yields for the reaction, $^{40}\text{Ar} + ^{58}\text{Fe}$ (circles), which has an intermediate value of the neutron-to-proton ratio, are in between those of the other two reactions. A similar feature is also observed for the $^{58}\text{Ni} + ^{58}\text{Fe}$, $^{58}\text{Fe} + ^{58}\text{Ni}$ and $^{58}\text{Fe} + ^{58}\text{Fe}$ reactions shown in Fig. 2. The fragment yield distributions therefore show the isospin dependence of the composite system on the fragments produced in the multifragmentation reaction. One also observes that the relative difference in the yield distribution between the three reactions in each figure decreases with increasing beam energy. This is due to the secondary de-excitation of the primary fragments, a process that becomes important for systems with increasing neutron-to-proton ratio and excitation energy.

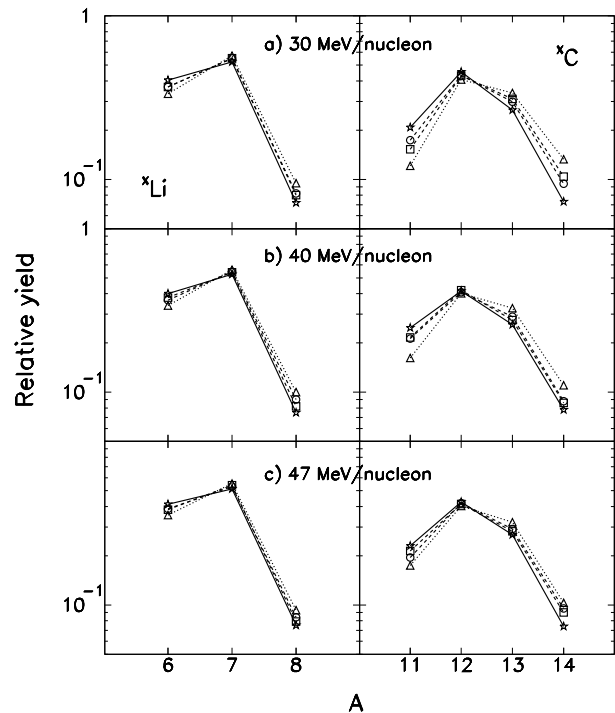


FIG. 2: Relative yield distribution of the fragments for the Lithium (left) and Carbon (right) isotopes in $^{58}\text{Ni} + ^{58}\text{Ni}$ (stars and solid lines), $^{58}\text{Fe} + ^{58}\text{Ni}$ (circles and dashed lines), $^{58}\text{Ni} + ^{58}\text{Fe}$ (squares and dashed lines), and $^{58}\text{Fe} + ^{58}\text{Fe}$ (triangles and dotted lines) reactions at various beam energies.

+ ^{58}Fe (triangle symbols) reactions, are shown in Fig. 2 for beam energies of 30, 40 and 47 MeV/nucleon. Similarly, the isotopic yield distributions for Lithium (left), Beryllium (center) and Carbon (right) elements, in $^{40}\text{Ca} + ^{58}\text{Ni}$ (star symbols), $^{40}\text{Ar} + ^{58}\text{Ni}$ (circle symbols) and $^{40}\text{Ar} + ^{58}\text{Fe}$ (square symbols) reactions, are shown in figure 3 for beam energies of 25, 33 and 45 MeV/nucleon. The isotope distribution for each element in Fig. 3 shows higher fragment yield for the neutron rich isotopes in $^{40}\text{Ar} + ^{58}\text{Fe}$ reaction (squares), which has the largest neutron-to-proton ratio (N/Z), in comparison to the $^{40}\text{Ca} + ^{58}\text{Ni}$ reaction (stars), which has the smallest neutron-to-proton ratio. The yields for the reaction, $^{40}\text{Ar} + ^{58}\text{Fe}$ (circles), which has an intermediate value of the neutron-to-proton ratio, are in between those of the other two reactions. A similar feature is also observed for the $^{58}\text{Ni} + ^{58}\text{Fe}$, $^{58}\text{Fe} + ^{58}\text{Ni}$ and $^{58}\text{Fe} + ^{58}\text{Fe}$ reactions shown in Fig. 2. The fragment yield distributions therefore show the isospin dependence of the composite system on the fragments produced in the multifragmentation reaction. One also observes that the relative difference in the yield distribution between the three reactions in each figure decreases with increasing beam energy. This is due to the secondary de-excitation of the primary fragments, a process that becomes important for systems with increasing neutron-to-proton ratio and excitation energy.

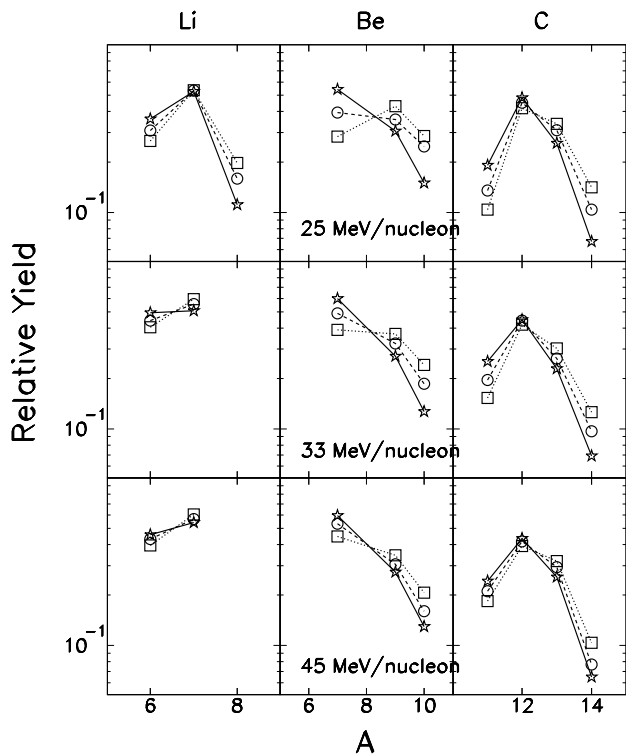


FIG. 3: Relative yield distribution of the fragments for Lithium (left), Beryllium (center) and Carbon (right) isotopes in $^{40}\text{Ca} + ^{58}\text{Ni}$ (stars and solid lines), $^{40}\text{Ar} + ^{58}\text{Ni}$ (circles and dashed lines), and $^{40}\text{Ar} + ^{58}\text{Fe}$ (squares and dotted lines) reactions at various beam energies.

B. Isotopic and Isotonic scaling

As discussed in section II, the ratio of isotope yields in two different systems, 1 and 2, $R_{21}(N, Z) = Y_2(N, Z)/Y_1(N, Z)$, follows an exponential dependence on the neutron number (N) and the proton number (Z) of the isotopes in relation known as isoscaling.

In Fig. 4, we show the isotopic yield ratio as a function of neutron number N , for Ar + Fe, Ar + Ni and Ca + Ni systems at beam energies of 25, 33, 45 and 53 MeV/nucleon. The left column shows the ratio for the $^{40}\text{Ar} + ^{58}\text{Fe}$ and $^{40}\text{Ca} + ^{58}\text{Ni}$ pair of reaction and the right column shows the ratio for the $^{40}\text{Ar} + ^{58}\text{Ni}$ and $^{40}\text{Ca} + ^{58}\text{Ni}$ pair of reaction. One observes that the ratio for each element shows linear behavior in the logarithmic plot and aligns with the neighboring element quite well. This feature is observed for all the beam energies and both pairs of reactions studied. One also observes that the alignment of the data points varies with beam energies as well as the pairs of reaction. To have a quantitative estimate of this variation, the ratio for each element (Z) was simultaneously fit using an exponential relation (shown by the solid lines) to obtain the slope parameter α . The values of the parameters are shown at the top of each panel in the figure. The value of the slope

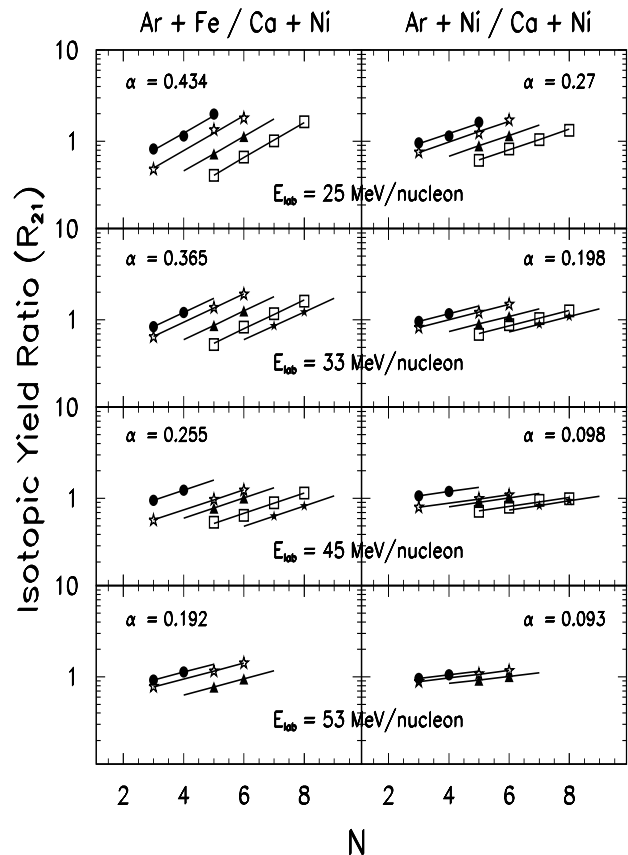


FIG. 4: Experimental isotopic yield ratios of the fragments as a function of neutron number N , for various beam energies. The left column correspond to $^{40}\text{Ar} + ^{58}\text{Fe}$ and $^{40}\text{Ca} + ^{58}\text{Ni}$ pair of reactions. The right column correspond to $^{40}\text{Ar} + ^{58}\text{Ni}$ and $^{40}\text{Ca} + ^{58}\text{Ni}$ pair of reactions. The different symbols correspond to $Z = 3$ (circles), $Z = 4$ (open stars), $Z = 5$ (triangles), $Z = 6$ (squares) and $Z = 7$ (filled stars) elements. The lines are the exponential fits to the data as explained in the text.

parameter α is larger for the $^{40}\text{Ar} + ^{58}\text{Fe}$ and $^{40}\text{Ca} + ^{58}\text{Ni}$ reactions, which has a larger difference in the N/Z of the systems in the pair, compared to the $^{40}\text{Ar} + ^{58}\text{Ni}$ and $^{40}\text{Ca} + ^{58}\text{Ni}$ reactions, which has a smaller difference in the corresponding N/Z . The α value furthermore decreases with increasing beam energy. A similar feature is also observed in Fe + Fe, Fe + Ni, Ni + Fe and Ni + Ni systems. Fig. 5 shows the isotope yield ratios and the isotone yield ratios for the Fe + Fe and Ni + Ni reactions for the 30 MeV/nucleon beam energy. A relative comparison of how the isoscaling parameter α , evolves as a function of beam energy and the isospin of the system is shown in Fig. 6. The figure clearly shows that the α value decreases with beam energy from 25 MeV/nucleon to 53 MeV/nucleon. In addition, there is also a clear drop in the α values with the decrease of the N/Z values of the system.

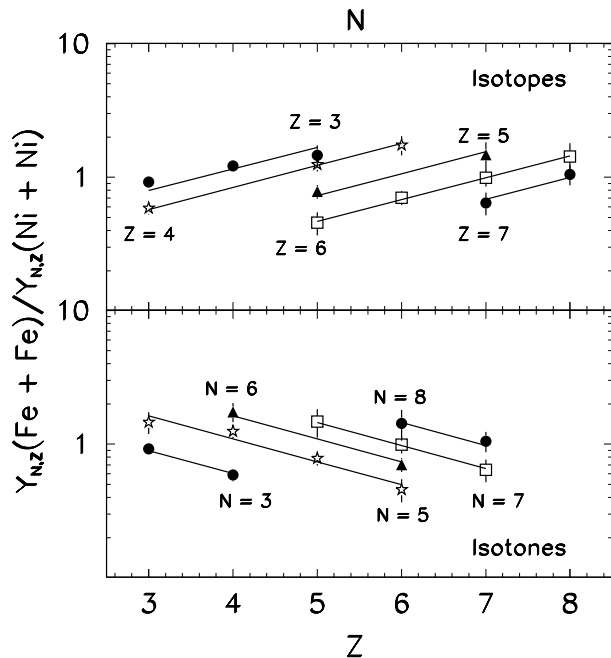


FIG. 5: Experimental isotope yield ratios (top) and isotone yield ratios (bottom) from $^{58}\text{Fe} + ^{58}\text{Fe}$ and $^{58}\text{Ni} + ^{58}\text{Ni}$ reactions as a function of N and Z for 30 MeV/nucleon beam energy. The solid lines are fit to the data as discussed in the text.

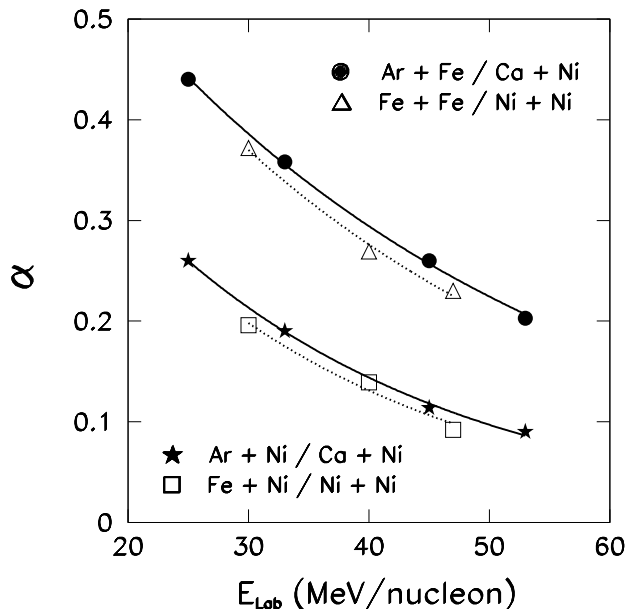


FIG. 6: Experimental isoscaling parameter α , as a function of the beam energy. The solid circles are for the $^{40}\text{Ar} + ^{58}\text{Fe}$ and $^{40}\text{Ca} + ^{58}\text{Ni}$ reactions. The open triangles are for $^{58}\text{Fe} + ^{58}\text{Fe}$ and $^{58}\text{Ni} + ^{58}\text{Ni}$ reactions. The solid stars are for $^{40}\text{Ar} + ^{58}\text{Ni}$ and $^{40}\text{Ca} + ^{58}\text{Ni}$ reactions. The open squares are for $^{58}\text{Fe} + ^{58}\text{Ni}$ and $^{58}\text{Ni} + ^{58}\text{Ni}$ reactions.

V. THEORETICAL MODEL COMPARISON

A. Dynamical AMD model

The Antisymmetrized Molecular Dynamics (AMD) [31, 43] is a microscopic model that simulates the time evolution of a nuclear collision. The colliding system in this model is represented in terms of a fully antisymmetrized product of Gaussian wave packets. During the evolution, the wave packet centroids move according to the deterministic equation of motion. The followed state of the simulation branches stochastically and successively into a huge number of reaction channels. The interactions are parameterized in terms of an effective force acting between nucleons and the nucleon-nucleon collision cross-sections. The advantage of using a dynamical model to study the nuclear equation of state is that it allows one to understand the functional form of the density dependence of the symmetry energy at a very fundamental level (*i.e.*, from the basic nucleon-nucleon interaction).

Recently [31], the fragment yields from heavy ion collisions simulated within the Antisymmetrized Molecular Dynamics (AMD) calculation were reported to follow a scaling behavior of the type shown in Eq. 1. A linear relation between the isoscaling parameter α and the difference in the isospin asymmetry $(Z/A)^2$ of the fragments (as given in Eq. 2), with appreciably different slopes, was predicted for two different forms of the density dependence of the symmetry energy; a “stiff” dependence (obtained from Gogny-AS interaction) and a “soft” dependence (obtained from Gogny interaction).

In this section, we compare the experimentally determined isoscaling parameter with the predictions of the AMD model calculation. The isospin asymmetry of the fragments for the present systems was estimated at $t = 300 \text{ fm}/c$ of the dynamical evolution using the AMD calculation. The values for the fragment asymmetry $(Z/A)^2$, were obtained by interpolating between those calculated for the $^{40}\text{Ca} + ^{40}\text{Ca}$, $^{48}\text{Ca} + ^{48}\text{Ca}$ and $^{60}\text{Ca} + ^{60}\text{Ca}$ systems by Ono *et al.* [31]. These systems are symmetric and nearly similar in charge and mass as studied in the present work. Fig. 7 shows the AMD calculation of the fragment asymmetry, $(Z/A)^2$ at $t = 300 \text{ fm}/c$, as a function of initial asymmetry at time $t = 0 \text{ fm}/c$, for two different choices of the nucleon-nucleon interaction, Gogny and Gogny-AS. The asymmetry values for the $^{40}\text{Ca} + ^{40}\text{Ca}$, $^{48}\text{Ca} + ^{48}\text{Ca}$ and $^{60}\text{Ca} + ^{60}\text{Ca}$ systems of Ref. [31] are shown by solid and hollow square symbols for the Gogny and Gogny-AS interaction, respectively. The lines are the linear fits to the calculations. The interpolated values for the present systems are shown by the solid circles and triangles, and hollow circles and triangles for the Gogny and Gogny-AS interaction, respectively.

We note that the AMD calculations carried out in Ref. [31] and shown in Fig. 7 correspond to the beam energy of 35 MeV/nucleon. The interpolated values of the asymmetries for the present systems obtained from Fig. 7 are

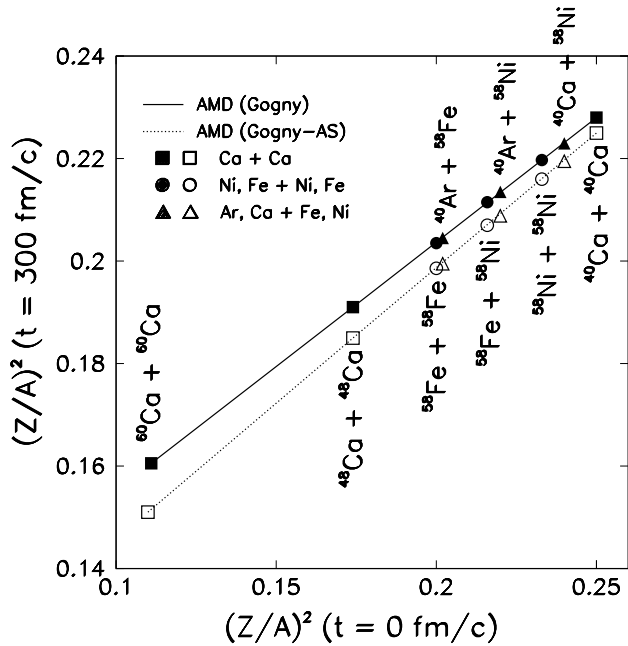


FIG. 7: AMD calculations of the fragment asymmetry $(Z/A)^2$, at $t = 300 \text{ fm}/c$ for the Gogny (solid line and solid squares) and Gogny-AS (dotted line and hollow squares) interactions at 35 MeV/nucleon. The calculations are taken from Ref. [31] for the systems shown by the square symbols. The lines are linear fit to the square symbols. The other symbols are the interpolated values for the systems studied in this work.

therefore for the beam energy of 35 MeV/nucleon. In order to compare the experimentally determined isoscaling parameter to that of the calculations, we therefore make use of the experimental isoscaling parameter for the beam energy of 35 MeV/nucleon using Fig. 6.

Fig. 8 shows a comparison between the experimentally observed α and those from the AMD model calculations plotted as a function of the difference in the fragment asymmetry for the beam energy of 35 MeV/nucleon. The solid and the dotted lines are the AMD model predictions for the “soft” (Gogny) and the “stiff” (Gogny-AS) form of the density dependence of the symmetry energy, respectively. The solid and the hollow symbols (squares, stars, triangles and circles) are the results of the present study for the two different values of the fragment asymmetry, assuming Gogny and Gogny-AS interactions, respectively. Also shown in the figure are the scaling parameters (asterisks, crosses, diamond and inverted triangle) taken from various other works in the literature [36, 49]. It is observed that the experimentally determined α parameter increases linearly with increasing difference in the fragment asymmetry of the two systems as predicted by the AMD calculation. Also, the data points are in closer agreement with those predicted by the Gogny-AS interaction (dotted line) than those from the usual Gogny force (solid line).

In the above comparison between the data and the cal-

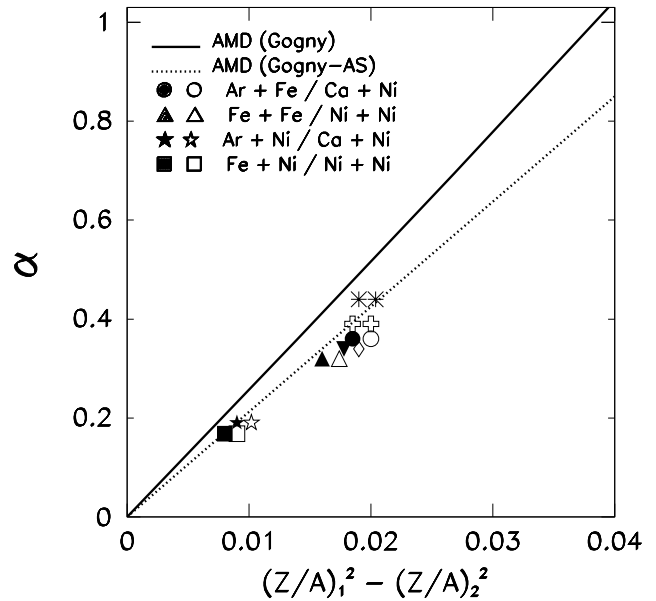


FIG. 8: Isoscaling parameter α , as a function of the difference in fragment asymmetry for 35 MeV/nucleon. The solid and the dotted lines are the AMD calculations for the Gogny and Gogny-AS interactions, respectively [31]. The solid and the hollow squares, stars, triangles and circles are from the present work as described in the text. The other symbols corresponds to data taken from [49] (asterisks) and [36] (crosses, diamonds, inverted triangles).

ulation, the corrections for the isoscaling parameter α due to the sequential de-excitation of the fragments are not taken into account. The slightly lower values of the isoscaling parameters (symbols) from the present measurements with respect to the Gogny-AS values (dotted line) could be due to the small secondary de-excitation effect of the fragments not accounted for in this comparison. Recently, it has been reported by Ono *et al.* [42], that the sequential decay effect in the dynamical calculations can affect the α value by as much as 50 %, and the ability to distinguish between the “stiff” and the “soft” form of the density dependence of the symmetry energy diminishes significantly. The calculations by Ono *et al.*, were carried out for the above studied systems using the AMD model. However, dynamical calculation carried out by Tian *et al.* [41], using Isospin Quantum Molecular Dynamic (IQMD) model shows no significant difference between the primary and the secondary α . The sequential decay effect from the IQMD calculation was also carried out for the same systems and beam energy as studied by Ono *et al.* [42] using the AMD model. The contrasting results between the two dynamical calculations for the same systems and energy currently present significant amount of uncertainty in reliably estimating the effect of sequential decay using dynamical models. One reason for this could be the large discrepancy that exists in the determination of the primary fragment exci-

tation energy from the current dynamical models. It has been shown using another dynamical model (stochastic mean field calculation) (see Liu *et al.* [33]), that it requires a significantly lower value of the primary fragment excitation energy (by as much as 50%), to be able to reproduce the experimentally observed fragment isotope distribution.

In the above comparison between the data and the calculation, we have therefore assumed the effect of the sequential decay to be negligible. A correction of about 10 - 15 %, as determined and well established from various statistical model studies [28], results in a slight increase in the α values bringing them even closer to the dotted line. The observed agreement of the experimental data with the Gogny-AS type of interaction therefore appears to suggest a “stiff” form of the density dependence of the symmetry energy.

Figure 9 shows various forms of the density dependence of the symmetry energy in isospin asymmetric nuclear matter used by Chen *et al.* [50], and those used in the present dynamical model analysis. The dot-dashed, dotted and the dashed curve corresponds to the momentum dependent Gogny interactions used by Chen *et al.*, to explain the NSCL-MSU isospin diffusion data. Assuming that the density dependence of the symmetry energy can be parametrized as,

$$C_{sym}(\rho) = C_{sym}^o \left(\frac{\rho}{\rho_o} \right)^\gamma \quad (3)$$

where C_{sym}^o , is the value of the symmetry energy at saturation density and γ is the parameter that characterizes the stiffness of the symmetry energy, the above dependences used by Chen *et al.* can be written as, $E_{sym} \approx 31.6 (\rho/\rho_o)^\gamma$, where, $\gamma = 1.6, 1.05$ and 0.69 , respectively. The solid curve and the solid point in Fig. 9 correspond to those from the Gogny and Gogny-AS interactions used to study the isoscaling data in the present work.

By parameterizing the density dependence of the symmetry energy that explains the present isoscaling data, one obtains, $C_{sym}(\rho) \approx 31.6 (\rho/\rho_o)^\gamma$, where $\gamma = 0.69$, from the dynamical model analysis.

B. Statistical Multifragmentation Model

The Statistical Multifragmentation Model (SMM) [51, 52] is based on the assumption of statistical equilibrium at a low density freeze-out stage. All breakup channels composed of nucleons and excited fragments are taken into account and considered as partitions. During each partition the conservation of mass, charge, energy, momentum and angular momentum is taken into account, and the partitions are sampled uniformly in the phase space according to their statistical weights using Monte Carlo sampling. The Coulomb interaction between the fragments is treated in the Wigner-Seitz approximation. Light fragments with mass number $A \leq 4$ are considered

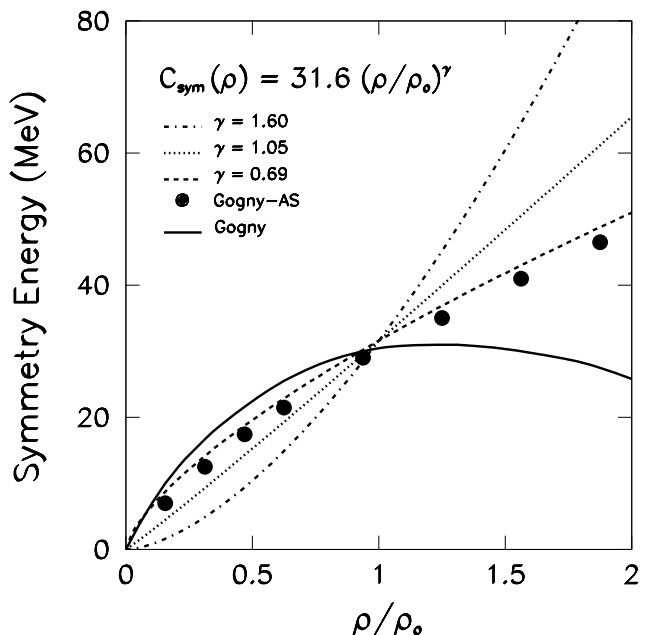


FIG. 9: Different forms of the density dependence of the nuclear symmetry energy used in the dynamical analysis of the present measurements on isoscaling data and the isospin diffusion measurements of NSCL-MSU [50]. The curves are as described in the text.

as elementary particles with only translational degrees of freedom (“nuclear gas”). Fragments with $A > 4$ are treated as heated nuclear liquid drops, and their individual free energies $F_{A,Z}$ are parametrized as a sum of the volume, surface, Coulomb and symmetry energy.

For the present study we make use of the SMM version adopted by Botvina *et al.* [36]. In this version, the secondary de-excitation of large fragments with $A > 16$ is described by Weisskopf-type evaporation and Bohr-Wheeler-type fission models [51, 53]. The decay of smaller fragments is treated with the Fermi-breakup model. All ground and nucleon-stable excited states of light fragments are taken into account and the population probabilities of these states are calculated according to the available phase space [53]. The sequential decay effect on the isoscaling parameter in this version of SMM has been established to be small and in good agreement with other versions of the statistical models.

Unlike dynamical calculations, the form of the density dependence of the symmetry energy is not known a priori, but has to be deduced from the systematic correlations between the isoscaling parameter, temperature, symmetry energy and the density of the multifragmenting system. To build this correlation, we make use of the fragment yield distributions measured in ^{58}Ni , $^{58}\text{Fe} + ^{58}\text{Ni}$, ^{58}Fe reactions at 30, 40 and 47 MeV/nucleon to study the isoscaling parameter α , as a function of the excitation energy of the fragmenting source. The parameter α was obtained from the ratio’s of the isotopic yields for two

different pairs of reactions, $^{58}\text{Fe} + ^{58}\text{Ni}$ and $^{58}\text{Ni} + ^{58}\text{Ni}$, and $^{58}\text{Fe} + ^{58}\text{Fe}$ and $^{58}\text{Ni} + ^{58}\text{Ni}$ as discussed in section 4.2. The excitation energy of the source for each beam energy was determined by simulating the initial stage of the collision dynamics using the Boltzmann-Nordheim-Vlasov (BNV) model calculation [54]. The results were obtained at a time around 40 - 50 fm/c after the projectile had fused with the target nuclei and the quadrupole moment of the nucleon coordinates (used for identification of the deformation of the system) approached zero. These excitation energies were also compared with those obtained from the systematic calorimetric measurements (see Ref. [55]) for systems with mass ($A \sim 100$), and similar to those studied in the present work, and are in good agreement. Fig. 10 (a) shows the experimental isoscaling parameter α , as a function of the excitation energy for Fe + Fe and Ni + Ni, and Fe + Ni and Ni + Ni pairs of reactions. A systematic decrease in the absolute values of the isoscaling parameter with increasing excitation energy is observed for both pairs. The α parameters for the $^{58}\text{Fe} + ^{58}\text{Fe}$ and $^{58}\text{Ni} + ^{58}\text{Ni}$ are about twice as large compared to those for the $^{58}\text{Fe} + ^{58}\text{Ni}$ and $^{58}\text{Ni} + ^{58}\text{Ni}$ pair of reactions.

The experimental isoscaling parameter was compared with the predictions of the Statistical Multifragmentation Model (SMM) [51, 56] calculations to study their dependence on the excitation energy and the isospin content. The initial parameters such as, the mass, charge and excitation energy of the fragmenting source for the calculation was obtained from the BNV calculations as discussed above. The possible uncertainties in the source parameters due to the loss of nucleons during pre-equilibrium emission was accounted for by carrying out the calculations for smaller source sizes. The break-up density in the calculation was taken to be multiplicity-dependent and was varied from approximately 1/2 to 1/3 the saturation density. This was achieved by varying the free volume with the excitation energy as shown in Ref. [51]. The form of the dependence was adopted from the work of Bondorf *et al.* [57, 58], (and shown by the solid curve in Fig. 10 (d)). It is known that the multiplicity-dependent break-up density, which corresponds to a fixed interfragment spacing and constant pressure at break-up, leads to a pronounced plateau in the caloric curve [57, 58]. A constant break-up density would lead to a steeper temperature versus excitation energy dependence.

The symmetry energy in the calculation was varied until a reasonable agreement between the calculated and the measured α was obtained. Fig. 10 (a) shows the comparison between the SMM calculated and the measured α for both pairs of systems. The dashed curves correspond to the calculation for the primary fragments and the solid curves to the secondary fragments. The width in the curve is the measure of the uncertainty in the inputs to the SMM calculation. It is observed that, within the given uncertainties, the decrease in the α values with increasing excitation energy and decreasing isospin difference $\Delta(Z/A)^2$, of the systems is well reproduced by

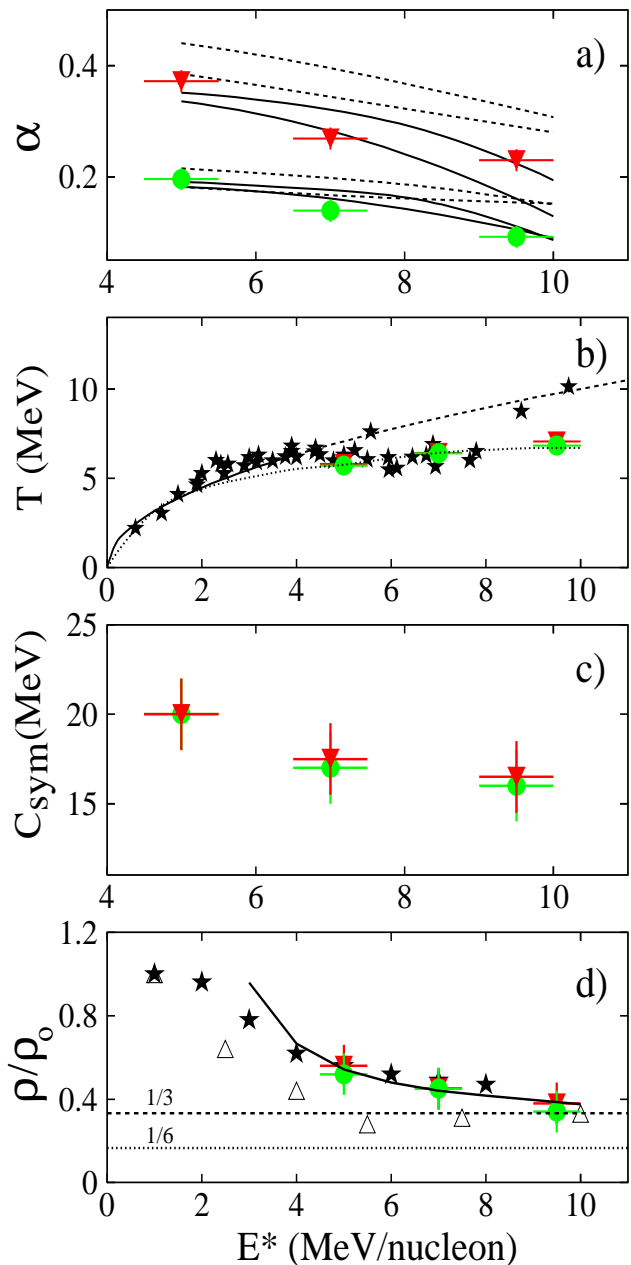


FIG. 10: (Color online) Isoscaling parameter α , temperature, symmetry energy and density as a function of excitation energy for the Fe + Fe and Ni + Ni (inverted triangles), and Fe + Ni and Ni + Ni (solid circles) reactions at 30, 40 and 47 MeV/nucleon. a) Experimental isoscaling parameter as a function of excitation energy. The solid and the dashed curves are the SMM calculations as discussed in the text. b) Temperature as a function of excitation energy. The solid stars correspond to the measured values and are taken from Ref. [55]. The solid and the dashed curve corresponds to the Fermi-gas relation. The dotted curve corresponds to the one obtained from Eq. 4. c) Symmetry energy as a function of excitation energy. d) Density as a function of excitation energy. The solid stars correspond to those from Ref. [69]. The open triangles are those from Ref. [70]. The solid curve is from Ref. [57].

the SMM calculation. One also notes that the effect of sequential decay on the isoscaling parameter is small as observed in several other studies [40, 59] using statistical models.

We show in Fig. 10 (b), the temperature as a function of excitation energy (*caloric curve*) obtained from the above SMM calculation that uses the excitation energy dependence of the break-up density to explain the observed isoscaling parameters. These are shown by the solid and inverted triangle symbols. Also shown in the figure are the experimentally measured caloric curve data compiled by Natowitz *et al.* [55], from various measurements for this mass range. The data from these measurements are shown collectively by solid star symbols and no distinction is made among them. The Fermi-gas model predictions with inverse level density parameter $K_o = 10$ (solid and dashed curve), is also shown. It is evident from the figure that the temperatures obtained from the SMM calculations are in good agreement with the overall trend of the caloric curve. Somewhat lower value for the temperature is observed when the break-up density of the system is kept constant at 1/3 the normal nuclear density. By allowing the break-up density to evolve with the excitation energy, a near plateau that agrees with the experimentally measured caloric curves is obtained. This assures that the input parameters used in the SMM calculation for comparing with the data are reasonable.

The symmetry energies obtained from the statistical model comparison of the experimental isoscaling parameter α , are as shown in Fig. 10 (c). A steady decrease in the symmetry energy with increasing excitation energy is observed for both pairs of systems. Such a decrease has also been observed in several other studies [60, 61, 62, 63]. We have also estimated the effect of the symmetry energy evolving during the sequential de-excitation of the primary fragments [60, 64]. These are reflected in the large error bars shown in Fig. 10 (c).

The phase diagram of the multifragmenting system is two dimensional and hence the excitation energy dependence of the temperature (the caloric curve) must take into account the density dependence too. Often this dependence is neglected while studying the caloric curve. In the following, we attempt to extract the density of the fragmenting system as a function of excitation energy. It has been shown by Sobotka *et al.* [65], that the plateau in the caloric curve could be a consequence of the thermal expansion of the system at higher excitation energy and decreasing density. By assuming that the decrease in the breakup density, as taken in the present statistical multifragmentation calculation, can be approximated by the expanding Fermi gas model, and furthermore the temperature in Eq. 2 and the temperature in the Fermi-gas relation are related, one can extract the density as a function of excitation energy using the relation

$$T = \sqrt{K_o(\rho/\rho_o)^{2/3}E^*} \quad (4)$$

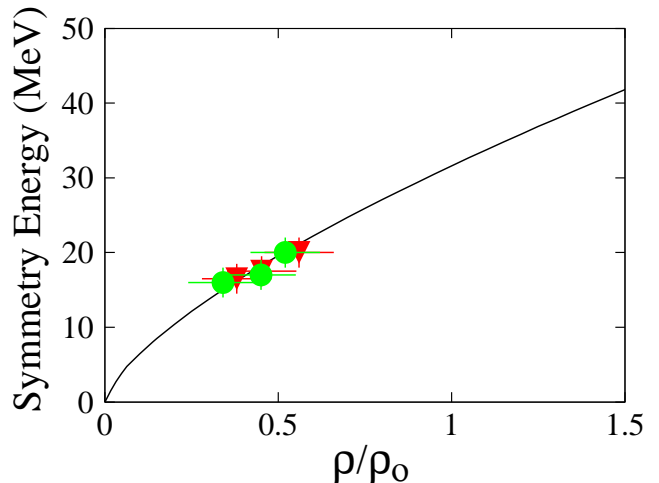


FIG. 11: (Color online) Symmetry energy as a function of density for the Fe + Fe and Ni + Ni pair of reaction (inverted triangles), and Fe + Ni and Ni + Ni pair of reactions (solid circles) for the 30, 40 and 47 MeV/nucleon. The solid curve is the dependence obtained from the dynamical model analysis as explained in the text.

In the above expression, the momentum and the frequency dependent factors in the effective mass ratio are taken to be one as expected at high excitation energies and low densities studied in this work [66, 67, 68].

The resulting densities for the two pairs of systems are shown in Fig. 10 (d) by the solid circles and inverted triangles. For comparison, we also show the break-up densities obtained from the analysis of the apparent level density parameters required to fit the measured caloric curve by Natowitz *et al.* [69], and those obtained by Viola *et al.* [70] from the Coulomb barrier systematics that are required to fit the measured intermediate mass fragment kinetic energy spectra. One observes that the present results obtained by requiring to fit the measured isoscaling parameters and the caloric curve are in good agreement with those obtained by Natowitz *et al.* The figure also shows the fixed freeze-out density of 1/3 (dashed line) and 1/6 (dotted line) of the saturation density assumed in various statistical model comparisons. The caloric curve obtained using the above densities and excitation energies (shown by solid stars, circles and the triangles) with $K_o = 10$ in Eq. 4, is shown by the dotted curve in Fig. 10 (b). The small discrepancy between the dotted curve and the data (solid stars) below 4 MeV/nucleon is due to the approximate nature of Eq. 4 being used.

It is therefore evident from figure 10 (a), (b), (c) and (d) that the decrease in the experimental isoscaling parameter α , symmetry energy, break-up density, and the flattening of the temperature with increasing excitation energy are all correlated. One can thus conclude that the expansion of the system during the multifragmentation process leads to a decrease in the isoscaling parameter, decrease in the symmetry energy and density, and the flattening of the caloric curve.

TABLE I: Parameterized form of the density dependence of the symmetry energy obtained from various independent studies.

Reference	Parametrization	Studies
Fuchs <i>et al.</i> [85]	$32.9(\rho/\rho_0)^{0.59}$	Relativistic Dirac-Brueckner calculation
Heiselberg <i>et al.</i> [82]	$32.0(\rho/\rho_0)^{0.60}$	Variational calculation
Danielewicz <i>et al.</i> [81]	$31(33)(\rho/\rho_0)^{0.55(0.79)}$	BE, skin, isospin analog states
Tsang <i>et al.</i> [79]	$12.125(\rho/\rho_0)^2$	Isospin diffusion
Chen <i>et al.</i> [50]	$31.6(\rho/\rho_0)^{1.05}$	Isospin diffusion
Li <i>et al.</i> [80]	$31.6(\rho/\rho_0)^{0.69}$	Isospin diffusion
Piekarewicz <i>et al.</i> [77, 78]	$32.7(\rho/\rho_0)^{0.64}$	Giant resonances
Shetty <i>et al.</i> [73, 74, 75]	$31.6(\rho/\rho_0)^{0.69}$	Isotopic distribution
Famiano <i>et al.</i> [87]	$32.0(\rho/\rho_0)^{0.55}$	neutron-proton emission ratio
Tsang <i>et al.</i> [28]	$23.4(\rho/\rho_0)^{0.6}$	Isotopic distribution

From the above correlation between the symmetry energy as a function of excitation energy, and the density as a function of excitation energy, we obtain the symmetry energy as a function of density. This is shown by the inverted triangles and solid circles in Fig. 11 for the Fe + Fe and Ni + Ni, and the Fe + Ni and Ni + Ni pair of reactions. The temperature in the present work remains nearly constant for the range of excitation energies studied, the observed decrease in the symmetry energy with increasing excitation energy is therefore a consequence of decreasing density. This is also supported by microscopic calculations which shows an extremely slow evolution of the symmetry energy with temperature [71, 72]. The evolution is practically negligible for the temperature range studied in this work. The solid curve in Fig. 11 corresponds to the dependence $C_{sym}(\rho) = 31.6 (\rho/\rho_0)^{0.69}$ MeV, obtained from the dynamical Anti-symmetrized Molecular Dynamic (AMD) calculation, as discussed in the previous section. It is thus observed that the dynamical and statistical models lead to similar density dependence of the symmetry energy.

VI. COMPARISON WITH OTHER INDEPENDENT STUDIES

In the following, we compare the form of the density dependence of the symmetry energy obtained from the present experimentally measured isoscaling parameter using the statistical and the dynamical multifragmentation models with several other recent independent studies. Fig. 12 shows this comparison. The green solid curve corresponds to the one obtained from Gogny-AS interaction in dynamical AMD model that explains the present results [73, 74], assuming the sequential decay effect to be small. The inverted triangle and the circle symbols also correspond to the present measurements obtained by comparing with the statistical multifragmentation model [75]. The red dashed curve corresponds to the one obtained recently from an accurately calibrated relativistic mean field interaction, used for describing the Gi-

ant Monopole Resonance (GMR) in ^{90}Zr and ^{208}Pb , and the IVGDR in ^{208}Pb by Piekarewicz *et al.* [76, 77, 78]. The pink dot-dashed curve correspond to the one used to explain the isospin diffusion results of NSCL-MSU using the isospin dependent Boltzmann-Uehling-Uhlenbeck (IBUU) model by Tsang *et al.* [79]. The blue dot-dashed curve also corresponds to the one used for explaining the isospin diffusion data of NSCL-MSU by Chen *et al.* [50], but with the momentum dependence of the interaction included in the IBUU calculation. This dependence has been further modified to include the isospin dependence of the in-medium nucleon-nucleon cross-section by Li *et al.* [80], and is in good agreement with the present study. The shaded region in the figure corresponds to those obtained by constraining the binding energy, neutron skin thickness and isospin analogue state in finite nuclei using the mass formula of Danielewicz [81]. The yellow solid curve correspond to the parameterization adopted by Heiselberg *et al.* [82] in their studies on neutron stars. By fitting earlier predictions of the variational calculations by Akmal *et al.* [83, 84], where the many-body and special relativistic corrections are progressively incorporated, Heiselberg and Hjorth-Jensen obtained a value of $C_{sym}^o = 32$ MeV and $\gamma = 0.6$, similar to those obtained from the present measurements. A similar result is also obtained from the relativistic Dirac-Brueckner calculation, with $C_{sym}^o = 32.9$ MeV and $\gamma = 0.59$ [85]. The Dirac-Brueckner is an “ab-initio” calculation based on nucleon-nucleon interaction with Bonn A type potential instead of the AV18 potential used in the variational calculation of Ref. [84]. The density dependence of the symmetry energy has also been studied in the framework of expanding emitting source (EES) model by Tsang *et al.* [28], where a power law dependence of the form $C_{sym}(\rho) = 23.4(\rho/\rho_0)^\gamma$, with $\gamma = 0.6$ was obtained. This dependence (shown by the black dotted curve) is significantly softer than other dependences shown in the figure. The solid square point in the figure correspond to the value of symmetry energy obtained by fitting the experimental differential cross-section data in a charge exchange reaction using the isospin dependent CDM3Y6 interaction of

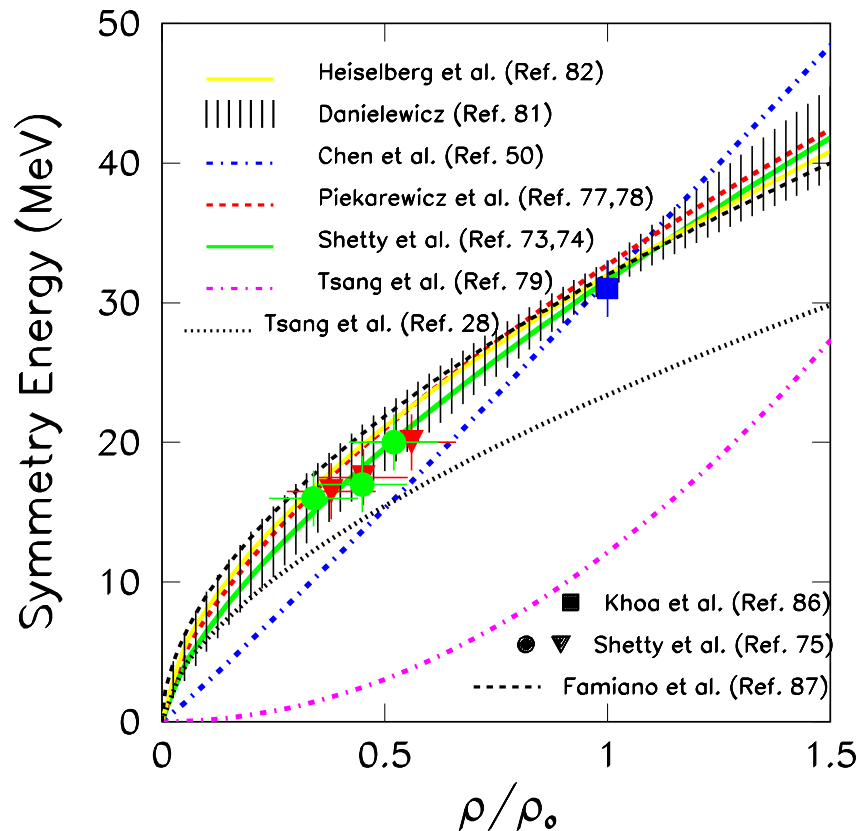


FIG. 12: (Color online) Comparison between the results on the density dependence of the symmetry energy obtained from various different studies. The various curves and the symbols are described in the text.

the optical potential by Khoa *et al.* [86].

An alternate observable, the double neutron/proton ratio of nucleons taken from two reaction systems using four isotopes of the same element, has recently been proposed as a probe to study the density dependence of the symmetry energy [87]. This observable is expected to be more robust than the isoscaling observable. It was shown recently [87] that the experimentally determined double-ratio for the $^{124}\text{Sn} + ^{124}\text{Sn}$ reaction to that for the $^{112}\text{Sn} + ^{112}\text{Sn}$ reaction, results in a dependence with $\gamma = 0.5$ (shown by black dashed curve in Fig. 12), when compared to the predictions of the IBUU transport model calculations. This observation is in close agreement with other studies discussed above. However, this dependence has been obtained by using the momentum independent calculation of Ref. [88]. A more recent calculation [89] using a BUU transport model that includes momentum dependent interaction show significantly lower values for the double neutron/proton ratio of free nucleons compared to the one reported by Famiano *et al.*

The parameterized forms of the density dependence of the symmetry energy obtained from all the above mentioned studies are as given in Table I. The close agreement between various independent studies show that a constraint on the density dependence of the symmetry energy, given as $C_{sym}(\rho) = C_{sym}^o(\rho/\rho_0)^\gamma$, where $C_{sym}^o \approx$

31 - 33 MeV and $\gamma \approx 0.55 - 0.69$ can be obtained.

VII. DISCUSSION

We make the following observations from the above comparison between the statistical and the dynamical model analysis :

1) *Assuming a negligibly small sequential decay effect, the form of the density dependence of the symmetry energy obtained from the dynamical model analysis is in good agreement with the one obtained from the statistical model analysis:* As mentioned earlier, the sequential decay effect among various dynamical model calculations is still a subject of debate. The statistical models however consistently show small sequential decay effect. If the sequential decay in both the dynamical and the statistical model is determined by the excitation energy, charge (Z) and mass (A) of the fragments, and not by the process that leads to these fragments, the de-excitation of the fragments must lead to a same amount of change in the isoscaling parameter (either a large change or no change at all). It is therefore unrealistic to assume that the sequential decay effect is different in the dynamical and the statistical model calculations. One comparison by Hudan *et al.* [90], show good agreement between the experimen-

tally determined primary fragment excitation energy and those calculated using the statistical multifragmentation model (see table II of Ref. [90]). Furthermore, if dynamical and statistical models are merely two different ways of interpreting the same multifragmentation process (*i.e.*, one simulating the entire process from the formation to the breakup stage, and the other simulating only the later breakup stage), the isoscaling parameter from both interpretation must lead to consistent results. It is well known, and as discussed in section II, that both interpretations predict isoscaling in multifragmentation. As discussed in section V A, the apparent disagreement between the sequential decay effect in statistical and dynamical models, could be due to the large discrepancy that exists in the determination of the primary fragment excitation energy from current dynamical models.

It has been argued [91] that the effect of sequential decay on the isoscaling parameter α , in statistical multifragmentation model depends not only on the excitation energy but also on the value of the symmetry energy. The fragments in their primary stage are usually hot and the properties of hot nuclei (*i.e.*, their binding energy and mass) differ from those of cold nuclei. If hot fragments in the freeze-out configuration have smaller symmetry energy, their mass at the beginning of the sequential de-excitation will be different and this effect should be taken into account. At smaller values of the symmetry energy the sequential decay effect can be large. In order to study the effect of symmetry energy evolution on isoscaling parameter during sequential decay, we have adopted in this work a phenomenological approach of Buyukcizmeci *et al.* [64]. Fig. 13 and 14 shows the primary and the secondary isoscaling parameter as a function of symmetry energy calculated from the statistical multifragmentation model (SMM) for the Ar + Ni and Ca + Ni, and Ar + Fe and Ca + Ni pair of reactions. The various panels from top to bottom correspond to different system excitation energies. Fig. 13 shows the result of the calculations where the symmetry energy is kept fixed, and Fig. 14 shows the result for the calculations where the symmetry energy is varied during the de-excitation process. The dashed lines in the figure correspond to the primary fragments (Eq. 2) and the solid lines to the secondary fragments. It is observed that there is no significant change in the primary and the secondary alpha.

2) *The result of the statistical model analysis is in good agreement with other independent studies*: A comparison between the density dependence of the symmetry energy obtained from the statistical model analysis (for which the sequential decay effect is known to be small) and other independent studies shows excellent agreement.

3) *The isoscaling parameter probes the property of infinite nuclear matter*: The symmetry energy obtained from dynamical model analysis (shown by the solid curve in Fig. 11) relates to the volume part of the symmetry energy as in infinite nuclear matter, whereas, the symmetry energy obtained from the statistical model analysis (solid circles and inverted triangles in Fig. 11) relates to the

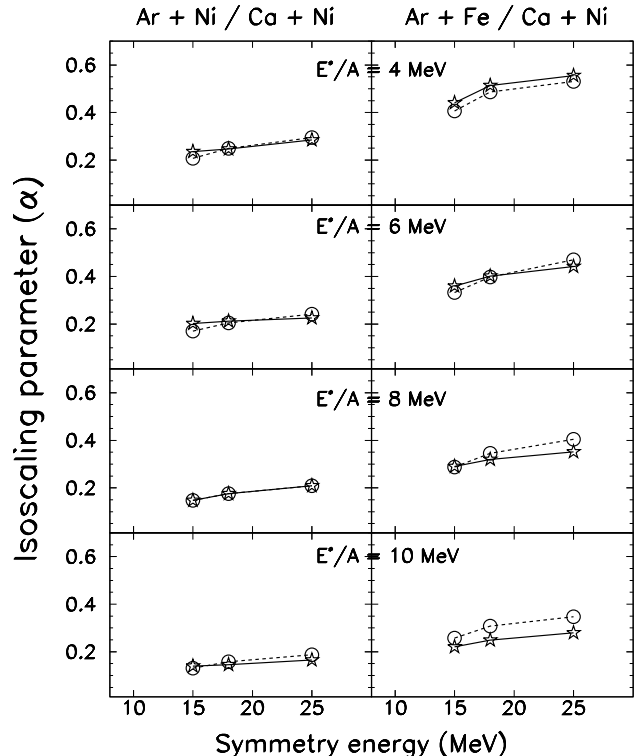


FIG. 13: SMM calculated isoscaling parameter α as a function of symmetry energy for various excitation energies. The open circles joined by dotted lines correspond to the primary fragments and the open stars joined by solid lines to the secondary fragments. The left column shows the calculation for $^{40}\text{Ar} + ^{58}\text{Ni}$ and $^{40}\text{Ca} + ^{58}\text{Ni}$ pair, and the right column for the $^{40}\text{Ar} + ^{58}\text{Fe}$ and $^{40}\text{Ca} + ^{58}\text{Ni}$ pair.

fragment that is finite and has surface contribution. The similarity between the two can probably be understood in terms of the weakening of the surface symmetry free energy when the fragments are being formed. During the density fluctuation in uniform low density matter, the fragments are not completely isolated and continue to interact with each other, resulting in a decrease in the surface contribution as predicted by Ono *et al.* [43]. It must be mentioned that by fitting the nuclear masses with mass formula, a volume contribution to the symmetry energy of about 31 - 33 MeV and surface contribution of about 11 - 13 MeV was obtained by Danielewicz [92] for nuclei at normal density. Using the constraint obtained for the volume part of the symmetry energy from the present study, and following the expression for the symmetry energy of finite nuclei by Danielewicz, we write the general expression for the density dependence of the symmetry energy as,

$$S_A(\rho) = \frac{\alpha(\rho/\rho_0)^\gamma}{1 + [\alpha(\rho/\rho_0)^\gamma/\beta A^{1/3}]} \quad (5)$$

where, $\alpha \equiv C_{sym}^0 = 31 - 33$ MeV, $\gamma = 0.55 - 0.69$ and $\alpha/\beta = 2.6 - 3.0$. The quantities α and β are the volume and the surface symmetry energy at normal nuclear density. The above equation reduces to Eq. 3 for infinite

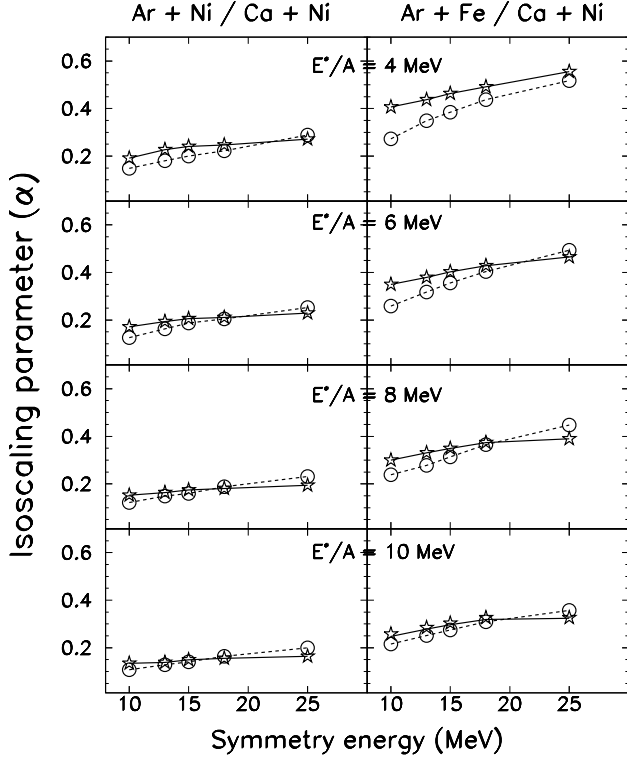


FIG. 14: Same as in fig. 13, but with the modified secondary de-excitation with evolving symmetry energy.

nuclear matter in the limit of $A \rightarrow \infty$, and to the symmetry energy of finite nuclei for $\rho = \rho_0$. The ratio of the volume symmetry energy to the surface symmetry energy (α/β) is closely related to the neutron skin thickness. Depending upon how the nuclear surface and the Coulomb contribution is treated, two different correlations between the volume and the surface symmetry energy have been predicted [17] from fits to nuclear masses. Experimental masses and neutron skin thickness measurements for nuclei with $N/Z > 1$ should provide tighter constraint on the surface-volume correlation.

4) *The density dependence of the symmetry energy obtained using the statistical model approach is consistent with other experimentally determined observables*: In the past, attempts have been made to study the density dependence of the symmetry energy by looking at specific observables and comparing them with the predictions of the dynamical models. Such an approach attempts to explain the observable of interest without trying to simultaneously explain other properties, such as, the temperature, density and excitation of the fragmenting system. This has led to a variety of different dependences without any clue to what density is being probed. It might not be straightforward to distinguish different realistic EOS interactions using dynamical models, due to the large uncertainties that currently exist in the sequential decay effects for these models. But the idea of extracting information on the symmetry energy from the point of view of the basic nucleon-nucleon interaction is a very pow-

erful approach. On the other hand, the determination of the density dependence of the symmetry energy from statistical model analysis by simultaneously explaining the isoscaling parameter, caloric curve and the density as a function of excitation energy is a reverse approach. This approach attempts to explain the experimental observables without any prior knowledge of the governing interaction and arrives at a dependence which can then be compared with those predicted from the basic interactions.

5) *Symmetry energy determined from the multifragmentation study is lower than that of normal nuclei*: Theoretical many-body calculations [1, 93, 94, 95] and those from the empirical liquid-drop mass formula [96, 97] predict symmetry energy near normal nuclear density and temperature to be around 30 - 32 MeV. Assuming a negligible evolution of the symmetry energy as a function of temperature, as shown in Ref. [71, 72], the present statistical model analysis yields symmetry energy of the order of 18 - 20 MeV at half the normal nuclear density.

6) *The above constraint on the density dependence of the symmetry energy has important implications for astrophysical and nuclear physics studies*:

a) *Neutron skin thickness*: It has been shown [98] that an empirical fit to a large number of mean-field calculations yield neutron skin thickness for ^{208}Pb nucleus, $R_n - R_p \simeq (0.22\gamma + 0.06) \text{ fm}$, where γ is the exponent that determines the stiffness of the density dependence of the symmetry energy. From the above comparison, assuming only those density dependences of the symmetry energy which have symmetry energy at normal nuclear density 31 - 33 MeV, one obtains a neutron skin thickness of 0.18 - 0.21 fm. An accurate determination of the neutron skin thickness from the parity-violating electron scattering measurement [18] will provide a unique observational constraint on the thickness of the neutron skin of a heavy nucleus. The above constraint also leads to symmetric matter nuclear compressibility of $K \sim 230$ MeV.

b) *Neutron star mass and radius*: The constraint also predicts a limiting neutron star mass of $M_{max} = 1.72$ solar mass and a radius, $R = 11 - 13 \text{ km}$ for the “canonical” neutron star. Recent observations of pulsar-white dwarf binaries at the Arecibo observatory suggest a pulsar mass for PSRJ0751+1807 of $M = 2.1_{-0.5}^{+0.4}$ solar mass at a 95% confidence level [99].

c) *Neutron star cooling*: Furthermore, it predicts a direct URCA cooling for neutron stars above 1.4 times the solar mass. If such is the case, then the enhanced cooling of a $M = 1.4$ solar mass neutron star may provide strong evidence in favor of exotic matter in the core of a neutron star.

These results have important implications for nuclear astrophysics and future experiments probing the properties of nuclei using beams of neutron-rich nuclei. The above constraint was obtained by studying the low density behavior of nuclear matter. Measurements at den-

sities above normal nuclear matter should further constrain the form of the symmetry energy. Such measurements should yield consistent results when extrapolated to low densities.

VIII. SUMMARY AND CONCLUSIONS

In summary, a number of reactions were studied to investigate the density dependence of the symmetry energy in the equation of state of isospin asymmetric nuclear matter. The results were analyzed within the framework of the dynamical and the statistical models of multifragmentation. It is observed that a dependence of the form $C_{sym}(\rho) = 31.6 (\rho/\rho_0)^{0.69}$ MeV, agrees reasonably with the experimental data indicating that a “stiff” form of the symmetry energy provides a better description of the

nuclear matter EOS at sub-nuclear densities. A comparison with several other independent studies shows that a constraint on the density dependence of the symmetry energy given as $C_{sym}(\rho) = C_{sym}^o(\rho/\rho_0)^\gamma$, where $C_{sym}^o \approx 31 - 33$ MeV and $\gamma \approx 0.55 - 0.69$, can thereby be obtained. The present observation has important implications for astrophysics, as well as, nuclear physics studies to be carried out at future radioactive beam facilities worldwide.

IX. ACKNOWLEDGMENTS

This work was supported in part by the Robert A. Welch Foundation through grant No. A-1266, and the Department of Energy through grant No. DE-FG03-93ER40773. We also thank A. Botvina for the SMM code, and the Catania group for the BNV code.

-
- [1] A.E.L. Dieperink, Y. Dewulf, D. Van Neck, M. Waroquier, and V. Rodin, *Phys. Rev. C* **68**, 064307 (2003).
 - [2] R.B. Wiringa, V. Fiks and A. Fabrocini, *Phys. Rev. C* **38**, 1010 (1988).
 - [3] C.H. Lee, T.T.S. Kuo, G.Q. Li and G.E. Brown, *Phys. Rev. C* **57**, 3488 (1998).
 - [4] B. Liu, V. Greco, V. Baran, M. Colonna, and M. DiToro, *Phys. Rev. C* **65**, 045201 (2002).
 - [5] N. Kaiser, S. Fritsch and W. Weise, *Nucl. Phys. A* **697**, 255 (2002).
 - [6] C. Fuchs and H.H. Wolter, *Eur. Phys. J. A* **30**, 5 (2006).
 - [7] B.A. Brown, *Phys. Rev. Lett* **85**, 5296 (2000).
 - [8] C.J. Horowitz and J. Piekarewicz, *Phys. Rev. Lett.* **86**, 5647 (2001).
 - [9] R.J. Furnstahl, *Nucl. Phys. A* **706**, 85 (2002).
 - [10] K. Oyamatsu, I. Tanihata, Y. Sugahara, K. Sumiyoshi, and H. Toki, *Nucl. Phys. A* **634**, 3 (1998).
 - [11] J. Lattimer, C. Pethick, M. Prakash and P. Hansel, *Phys. Rev. Lett.* **66**, 2701 (1991).
 - [12] C. Lee, *Phys. Rep.* **275**, 255 (1996).
 - [13] C.J. Pethick and D.G. Ravenhall, *Annu. Rev. Nucl. Part. Sci.* **45**, 429 (1995).
 - [14] J.M. Lattimer and M. Prakash, *Phys. Rep.* **333**, 121 (2000).
 - [15] W.R. Hix, O.E.B. Messer, A. Mezzacappa, M. Liebendorfer, J. Sampaio, K. Langanke, D.J. Dean, and G. Martinez-Pinedo, *Phys. Rev. Lett.* **91**, 201102 (2003).
 - [16] J.M. Lattimer and M. Prakash, *Science*, **304**, 536 (2004).
 - [17] A.W. Steiner, M. Prakash, J.M. Lattimer and P.J. Ellis, *Phys. Rep.* **411**, 325 (2005).
 - [18] C.J. Horowitz, S.J. Pollock, P.A. Souder and R. Michaels, *Phys. Rev. C* **63**, 025501 (2001).
 - [19] C.J. Horowitz and J. Piekarewicz, *Phys. Rev. C* **66**, 55803 (2002).
 - [20] J.R. Stone, J.C. Miller, R. Koncewicz, P.D. Stevenson and M.R. Strayer, *Phys. Rev. C* **68**, 034324 (2003).
 - [21] J. Lattimer *et al.*, *Astrophys. J.* **425**, 802 (1994).
 - [22] P. Slane, D.J. Helfand and S.S. Murray, *Astrophys. J. L* **571**, 45 (2002).
 - [23] P. Danielewicz, R. Lacey and W.G. Lynch, *Science*, **298**, 1592 (2002).
 - [24] GSI Conceptual Design Report, <http://www.gsi.de/GSI-Future>.
 - [25] RIA homepage, <http://www.orau.org/ria>.
 - [26] B.A. Li, C.M. Ko and W. Bauer, *Int. J. Mod. Phys. E* **7**, 147 (1998).
 - [27] V. Baran, M. Colonna, V. Greco and M. DiToro, *Phys. Rep.* **410**, 335 (2005).
 - [28] M.B. Tsang, W.A. Friedman, C.K. Gelbke, W.G. Lynch, G. Verde, and H.S. Xu, *Phys. Rev. Lett.* **86**, 5023 (2001).
 - [29] H.S. Xu *et al.*, *Phys. Rev. Lett.* **85**, 716 (2000).
 - [30] D.V. Shetty, S.J. Yennello, E. Martin, A. Keksis, G.A. Souliotis, *Phys. Rev. C* **68**, 021602 (2003).
 - [31] A. Ono, P. Danielewicz, W.A. Friedman, W.G. Lynch and M.B. Tsang, *Phys. Rev. C* **68**, 051601 (2003).
 - [32] Q. Li, Z. Li, H. Stocker, *Phys. Rev. C* **73**, 051601 (2006).
 - [33] T.X. Liu *et al.*, *Phys. Rev. C* **69**, 014603 (2004).
 - [34] M. Colonna and F. Matera, *Phys. Rev. C* **71**, 064605 (2005).
 - [35] C.O. Dorso, C.R. Escudero, M. Ison, and J.A. Lopez, *Phys. Rev. C* **73**, 044601 (2006).
 - [36] A.S. Botvina, O.V. Lozhkin and W. Trautmann, *Phys. Rev. C* **65**, 044610 (2002).
 - [37] A.I.H. Raduta, Ad.R. Raduta, *Phys. Rev. C* **65**, 054610 (2002).
 - [38] W.A. Friedman, *Phys. Rev. C* **42**, 667 (1990).
 - [39] D.H.E. Gross, *Phys. Rep.* **279**, 119 (1997).
 - [40] M.B. Tsang *et al.*, *Phys. Rev. C* **64**, 054615 (2001).
 - [41] W.D. Tian *et al.*, arXiv: nucl-th/0601079 (2006).
 - [42] A. Ono, P. Danielewicz, W.A. Friedman, W.G. Lynch and M.B. Tsang, arXiv: nucl-ex/0507018 (2005).
 - [43] A. Ono, P. Danielewicz, W.A. Friedman *et al.*, *Phys. Rev. C* **70**, 041604 (2004).
 - [44] H. Johnston *et al.*, *Phys. Rev. C* **56**, 1972 (1997).
 - [45] S.J. Yennello *et al.*, *Phys. Lett. B* **321**, 15 (1994).
 - [46] R.P. Schmitt *et al.*, *Nucl. Instrum. Methods Phys. Res. A* **354**, 487 (1995).
 - [47] C.A. Ogilvie, D.A. Cebra, J. Clayton, S. Howden, J. Karn, A. Vander Molen, G.D. Westfall, W.K. Wilson, and J.S. Winfield, *Phys. Rev. C* **40**, 654 (1989).
 - [48] S.J. Yennello *et al.*, *Proc. of the 10th Winter Workshop on Nuclear Dynamics, Snowbird, UT*, edited by W. Bauer

- (1994).
- [49] E. Geraci *et al.*, Nucl. Phys. A **732**, 173 (2004).
- [50] L.W. Chen, C.M. Ko and B.A. Li, Phys. Rev. Lett. **94**, 032701 (2005).
- [51] J.P. Bondorf *et al.*, Phys. Rep. **257**, 133 (1995).
- [52] A.S. Botvina *et al.*, Nucl. Phys. A **584**, 737 (1995).
- [53] A.S. Botvina, A.S. Iljinov, I.N. Mishustin, J.P. Bondorf, R. Donangelo, and K. Sneppen, Nucl. Phys. A **475**, 663 (1987).
- [54] V. Baran, M. Colonna, M. Di Toro, V. Greco, M. Zielinska-Pfabe and H.H. Wolter, Nucl. Phys. A **703**, 603 (2002).
- [55] J.B. Natowitz, R. Wada, K. Hagel, T. Keutgen, M. Murray, A. Makeev, L. Qin, P. Smith, and C. Hamilton, Phys. Rev. C **65**, 034618 (2002); *and references therein*.
- [56] A.S. Botvina and I.N. Mishustin, Phys. Rev. C **63**, 061601 (2001).
- [57] J.P. Bondorf, R. Donangelo, I.N. Mishustin and H. Schultz, Nucl. Phys. A **444**, 460 (1985).
- [58] J.P. Bondorf, A.S. Botvina and I.N. Mishustin, Phys. Rev. C **58**, 27 (1998).
- [59] W.P. Tan *et al.*, Phys. Rev. C **64**, 051901 (2001).
- [60] J. Iglio, D.V. Shetty, S.J. Yennello, G.A. Souliotis, M. Jandel, A. Keksis, S. Soisson, B. Stein and S. Wuenschel, Phys. Rev. C **74**, 024605 (2006).
- [61] D.V. Shetty, A.S. Botvina, S.J. Yennello, A. Keksis, E. Martin and G.A. Souliotis, Phys. Rev. C **71**, 024602 (2005).
- [62] A. LeFevre *et al.*, Phys. Rev. Lett. **94**, 162701 (2005).
- [63] D. Henzlova, A.S. Botvina, K.H. Schmidt, V. Henzl, P. Napolitani, and M.V. Ricciardi, arXiv: nucl-ex/0507003 (2005).
- [64] N. Buyukcizmeci, R. Ogul, and A.S. Botvina, Eur. Phys. J. **25**, (2005) 57.
- [65] L.G. Sobotka, R.J. Charity, J. Toke and W.U. Schroder, Phys. Rev. Lett. **93**, 132702 (2004).
- [66] R. Hasse and P. Schuck, Phys. Lett. B **179**, 313 (1986).
- [67] S. Shlomo and J.B. Natowitz, Phys. Lett. B **252**, 187 (1990).
- [68] S. Shlomo and J.B. Natowitz, Phys. Rev. C **44**, 2878 (1991).
- [69] J.B. Natowitz, K. Hagel, Y. Ma, M. Murray, L. Qin, S. Shlomo, R. Wada, and J. Wang, Phys. Rev. C **66**, 031601 (2002).
- [70] V.E. Viola, K. Kwiatkowski, J.B. Natowitz, and S.J. Yennello, Phys. Rev. Lett. **93**, 132701 (2004).
- [71] *Isospin Physics in Heavy Ion Collisions at Intermediate Energies*, edited by B.-A. Li and W. Schroder (Nova Science, New York, 2001).
- [72] B.A. Li and L.W. Chen, Phys. Rev. C **74**, 034610 (2006).
- [73] D.V. Shetty, S.J. Yennello, A.S. Botvina, G.A. Souliotis, M. Jandel, E. Bell, A. Keksis, S. Soisson, B. Stein, and J. Iglio, Phys. Rev. C **70**, 011601 (2004).
- [74] D.V. Shetty, S.J. Yennello, and G.A. Souliotis, Phys. Rev. C **75**, 034602 (2007); arXiv: nucl-ex/0505011 (2005).
- [75] D.V. Shetty, S.J. Yennello, G.A. Souliotis, A.L. Keksis, S.N. Soisson, B.C. Stein, and S. Wuenschel, Phys. Rev. C (2007) (Submitted); arXiv: nucl-ex/0606032 (2006).
- [76] B.G. Todd-Rutel and J. Piekarewicz, Phys. Rev. Lett **95**, 122501 (2005).
- [77] J. Piekarewicz (Private Communication).
- [78] J. Piekarewicz, *Proc. of the International Conference on Current Problems in Nuclear Physics and Atomic Energy, Kyiv, Ukraine, (May 29 - June 3, 2006)*.
- [79] M.B. Tsang *et al.*, Phys. Rev. Lett. **92**, 062701 (2004).
- [80] B.A. Li and L.W. Chen, Phys. Rev. C **72**, 064611 (2005).
- [81] P. Danielewicz, arXiv : nucl-th/0411115 (2004).
- [82] H. Heiselberg and M. Hjorth-Jensen, Phys. Rep. **328**, 237 (2000).
- [83] A. Akmal and V.R. Pandharipande, Phys. Rev. C **56**, 2261 (1997).
- [84] A. Akmal, V.R. Pandharipande and D.G. Ravenhall, Phys. Rev. C **58**, 1804 (1998).
- [85] C. Fuchs (Private Communication); E.N.E. van Dalen, C. Fuchs, and A. Faessler, Nucl. Phys. A **744**, 227 (2004).
- [86] D.T. Khoa and H.S. Than, Phys. Rev. C **71**, 044601 (2005).
- [87] M.A. Famiano *et al.*, Phys. Rev. Lett. **97**, 052701 (2006).
- [88] B.A. Li, C. Ko, and Z. Ren, Phys. Rev. Lett. **78**, 1644 (1997).
- [89] B.A. Li, L.W. Chen, G.C. Yong, and W. Zuo, Phys. Lett. B **634**, 378 (2006).
- [90] S. Hudan *et al.*, Phys. Rev. C **67**, 064613 (2003).
- [91] M. Colonna and M.B. Tsang, Eur. Phys. J. A **30**, 165 (2006).
- [92] P. Danielewicz, Nucl. Phys. A **727**, 233 (2003).
- [93] W. Zuo, I. Bombaci, and U. Lombardo, Phys. Rev. C **60**, 024605 (1999).
- [94] M. Brack, C. Guet, and H.B. Hakansson, Phys. Rep. **123**, 276 (1985).
- [95] J.M. Pearson and R.C. Nayak, Nucl. Phys. A **668**, 163 (2000).
- [96] W.D. Myers and W.J. Swiatecki, Nucl. Phys. **81**, 1 (1966).
- [97] K. Pomorski and J. Dudek, Phys. Rev. C **67**, 044316 (2003).
- [98] C.J. Horowitz, Eur. Phys. J. A **30**, 303 (2006).
- [99] D.J. Nice *et al.*, Astrophys. J. **634**, 1242 (2005).